The Effects of Sweeping Jet Actuator Parameters on Flow Separation Control

Mehti Koklu[1]
NASA Langley Research Center, Hampton, VA 23681

A parametric experimental study was performed with sweeping jet actuators (fluidic oscillators) to determine their effectiveness in controlling flow separation on an adverse pressure gradient ramp. Actuator parameters that were investigated include blowing coefficients, operation mode, pitch and spreading angles, streamwise location, aspect ratio, and scale. Surface pressure measurements and surface oil flow visualization were used to characterize the effects of these parameters on the actuator performance. 2D Particle Image Velocimetry measurements of the flow field over the ramp and hot-wire measurements of the actuator's jet flow were also obtained for selective cases. In addition, the sweeping jet actuators were compared to other well-known flow control techniques such as micro-vortex generators, steady blowing, and steady vortex-generating jets. The results confirm that the sweeping jet actuators are more effective than steady blowing and steady vortex-generating jets. The results also suggest that an actuator with a larger spreading angle placed closer to the location where the flow separates provides better performance. For the cases tested, an actuator with an aspect ratio, which is the width/depth of the actuator throat, of 2 was found to be optimal. For a fixed momentum coefficient, decreasing the aspect ratio to 1 produced weaker vortices while increasing the aspect ratio to 4 reduced coverage area. Although scaling down the actuator (based on the throat dimensions) from 0.25 inch x 0.125 inch to 0.15 inch x 0.075 inch resulted in similar flow control performance, scaling down the actuator further to 0.075 inch x 0.0375 inch reduced the actuator efficiency by reducing the coverage area and the amount of mixing in the near-wall region. The results of this study provide insight that can be used to design and select the optimal sweeping jet actuator configuration for flow control applications.

Nomenclature

APG	=	adverse-pressure gradient
C_μ	=	momentum coefficient
C_π	=	power coefficient
C_p	=	pressure coefficient
MVG	=	micro-vortex generator
NFC	=	no flow control
P	=	actuator plenum pressure, psid
Q	=	actuator volume flow rate, cubic feet per second
SWJ	=	sweeping jet
U_∞	=	free-stream velocity, feet/second
VGJ	=	vortex-generating jet
VR	=	jet-to-free-stream velocity ratio
X_{SWJ}	=	actuator-streamwise location
α	=	pitch angle, degrees
δ	=	boundary-layer thickness, inches
θ	=	spreading angle, degrees

[1] Research Engineer, Flow Physics and Control Branch, MS 170, Member AIAA.

I. Introduction

One of the technical challenges of the NASA Fixed Wing Project is to reduce aircraft drag with minimal impact on cruise performance.[1] Reducing the drag not only improves aerodynamic efficiency, but also improves the fuel efficiency of an aircraft thereby reducing emissions and operating costs. One viable approach to reduce drag is to reduce the wetted area of aircraft components while maintaining aerodynamic performance. This can be accomplished on an aircraft wing through the use of high-lift systems. High-lift systems enable a more efficient wing in flight while adding more lift for takeoff and landing operations; however, they are vulnerable to flow separation at high angles of attack and large flap deflections. Developing methods to control the flow separation could help simplify the high lift systems, which in turn, could help reduce drag and overall weight.

Flow separation control methods are usually designed to delay or completely eliminate separation by energizing the decelerated near-wall fluid by adding either momentum or vorticity to the boundary layer. Near-wall momentum addition in the form of blowing has been a preferred and straightforward separation control technique that has been studied extensively.[2] An alternate approach involves adding streamwise vorticity to increase the boundary layer mixing and enhances the convective transport of the free-stream momentum towards the near wall. Vorticity addition can be either passive or active. Passive micro-vortex generators (MVGs)[3] have been successfully utilized in both low-speed[4, 5] and high-speed[6] applications to control the boundary layer. Lin[7] performed a detailed review of vortex generator studies that used MVGs to control boundary-layer separation. Active vortex generating methods such as vortex-generating jets (VGJs)[8] provide the benefit of passive vortex generators without having the associated drag penalty. VGJs also provide an opportunity to adjust the flow control parameters to accommodate changing flow conditions.

Sweeping jet (SWJ) actuators, i.e., fluidic oscillators have been the subject of much research in the active flow control field due to their unique design features such as nomoving parts, a simple structure, limited maintenance requirements, dimensional scalability, and high-frequency and high-momentum bandwidth. These actuators emit spatially and temporally oscillating jets without having any electromechanical moving components. In their recent review, Gregory and Tomac[9] provided a brief history of the fluidic oscillators from their development as fluid amplifiers to their current usage as flow control actuators. Internal and external flow structures created by a similar SWJ actuator used in the present study were investigated both experimentally and numerically.[10, 11] Koklu and Melton[12] also studied the flow field produced by a SWJ actuator using hot-wire anemometry and particle image velocimetry (PIV) measurements and compared the jet characteristics to that of a turbulent free jet. They reported that SWJ actuators produce wider jet spreading and higher velocity fluctuations compared to the turbulent free jets and act as vortex-generating jets in failure modes.[12] SWJ actuators were successfully used to control flow separation on an adverse pressure gradient (APG) ramp.[13] It was revealed that the SWJ actuators are more efficient than steady blowing using straight and angled jets (VGJs). A number of studies in the literature showed that SWJ actuators are reliable and efficient flow control devices for improving aerodynamic performance. These studies include, but are not limited to the application of SWJ actuators on a 30° swept wing high-lift model,[14] a V-22 wing-nacelle combination,[15] wind turbine blades,[16] trucks,[17] bluff bodies,[18] and recently a full-scale Boeing 757 vertical tail model.[19]

The current study is a continuation of a previous study reported in Ref. 13, where SWJ actuators was evaluated and compared to other types of flow control methods. In that study, the effects of actuator aspect ratio and blowing rate on flow separation control were investigated. In addition to aspect ratio and blowing rate, this study will examine the effects of actuator operation mode, actuator placement, and actuator size on the performance of the SWJ actuator in controlling flow separation. The effect of each parameter will be evaluated and compared to determine an efficient actuator configuration. Surface pressure measurements and surface flow visualization will be presented to show the effects of these parameters. For some selected cases, 2D PIV measurements of the flow field over the APG ramp and hot-wire measurements of the actuator's jet velocity will be provided and discussed.

II. Experimental Setup

A. Facility and Instrumentation

The experiments in this study were conducted in the NASA Langley 15-Inch Low Speed Tunnel in support of the NASA Fixed Wing Project. The description of the tunnel was previously reported in Refs. 4 and 13. The tunnel is a closed return, atmospheric facility used primarily for fundamental flow physics research. The tunnel test section is 15 inches by 15 inches. The wind tunnel model consists of a long aluminum splitter plate with an APG ramp model placed between Stations 58 and 75 (see Fig. 1). The station numbers correspond to the distance from the leading edge of the splitter plate in inches. The model geometry was a Stratford ramp with incipient flow separation.

Adverse pressure gradient created by the ramp model caused corner vortices to be formed in the tunnel sidewalls. The boundary layer was tripped near the leading edge of the splitter-plate to produce a turbulent boundary layer. The pressure distribution over the upper splitter plate was adjusted to be uniform between Stations 20 and 50 using supports in the upper tunnel wall to slightly modify the ceiling geometry. Although the same wind tunnel and ramp model described in Ref. 13 were used, there were slight differences in the experimental configurations. One of the differences was the position of the splitter-plate flap, which is used to eliminate a separation bubble from forming on the leading edge of the splitter plate. Since the leading edge of the splitter plate is a thick airfoil, incoming flow does not generate any leading edge separation. Therefore, the splitter-plate flap was modified to be at non-deflected position. Although the different flap configurations resulted in different flow conditions on the ramp model, all of the experiments presented in this study were performed using the same configuration. Another difference in the experimental setup was the location of the pitot-static probe. Previously, the pitot-static probe was located in front of the splitter plate to measure the tunnel velocity. The onset flow velocity upstream of the ramp model was estimated from the tunnel velocity. In the current configuration, the pitot-static probe was installed near Station 26 to provide a direct measure of the freestream velocity in the test section upstream of the ramp.

The ramp model was instrumented with 45 surface static pressure ports (0.020-inch ID) located along the centerline and laterally across the ramp at selected stations. The spanwise distribution at each station consisted of five-pressure ports equally spaced at 0.5-inch intervals around the centerline of the ramp. The pressure ports were connected to an electronically scanned pressure (ESP) module that communicated with a computer via Ethernet. The pressure transducer in the acquisition module can record a maximum of 1 psid with an accuracy of ±0.06 psi. Surface pressure data presented in this study were obtained by ensemble averaging 6400 pressure signals from each pressure port to provide excellent accuracy and filtering.

A previously developed flow visualization technique was used in this study. This technique used a mixture of kerosene, aviation oil, and fumed silica particles. Details of the flow visualization technique can be found in Ref. 13. In this technique, the mixture was applied to black contact paper mounted on the ramp model. As the tunnel speed was adjusted to the specified test conditions, the mixture moved under the effect of local shear stresses and revealed the surface flow topology. Fluorescent pigment in the aviation oil glowed under UV lighting and produced vivid flow visualization images.

Time-averaged velocity field measurements were made using a 2D PIV system for selected cases. The PIV images were recorded using a 2560 pixel x 1600 pixel camera with a 55 mm macro lens. The field of view was approximately 12 inches wide by 7.5 inches tall covering the entire APG ramp region (from Station 61.5 to Station 73.5) along the tunnel centerline. The light sheet was produced by a Nd:YLF dual cavity-high speed laser (2 x 30 mJ/pulse) operated at 0.7 kHz repetition rate. The flow was seeded with 1-micron particles produced by a commercial fog generator. For the data presented, 1000 image pairs were used to compute the time-averaged values. The data were processed using commercially available PIV analysis software.[20]

B. Flow Control Methods and Parameters

In order to provide a reference flow control case, an array of MVGs was used as a passive flow control device. The centerline pressure (C_p) distribution obtained using MVG flow control was used as a target C_p distribution for the SWJ actuators. The MVGs were low-profile, trapezoidal-shaped with 3/16-inch height and 3/4-inch length similar to that described in Ref. 4. There were six counter-rotating MVGs installed at Station 58 and oriented at ±23° angles with respect to the direction of the freestream flow. Figure 2 shows the spanwise distribution of MVGs relative to the SWJ actuator exits. This particular (six counter-rotating MVG) configuration was selected to make an unbiased comparison with the SWJ actuator array.

An array of SWJ actuators comprised of three-SWJ actuators (Fig. 2) was used as an active flow control device to control flow separation on the APG ramp. The actuator array was arranged in a lateral line pattern such that the center of the middle actuator was positioned at the tunnel centerline (Fig. 1). The spacing between two adjacent SWJ actuators was 2.5 inches. The actuator array was fabricated from acrylic material with a CNC machine. For the baseline configuration, the actuator array was installed at Station 58 similar to MVGs. The actuator exits were flush with the splitter-plate surface. The jet axis of the SWJ actuators pointed downstream at an angle of 30° to the freestream flow. The throat of the SWJ actuators was 0.25-inch wide by 0.125-inch deep. Each actuator in the array shared the same plenum. The flow rate to the actuator array was controlled by a flow meter and held constant during the experiment. The actuator parameters such as blowing coefficient, operation mode, pitch and spreading angles, streamwise location, aspect ratio, and scale were changed one at a time from the baseline configuration to determine the effectiveness of each parameter in controlling flow separation.

The most important parameter for an active flow control device is the blowing coefficient. The momentum coefficient, C_μ, is frequently used in the literature and defined as $C_\mu = 2 * VR^2 * \frac{A_{jet}}{A_{ref}}$, where VR is the ratio of the jet exit velocity to the freestream velocity, A_{jet} is the total area of the actuator throats, and A_{ref} is the reference area. In this study, the reference area is the area of the separated region. This definition of C_μ is true for incompressible flows. Because the velocity out of the SWJ actuator (measured and found to be 224 feet/second for the majority of the cases) was less than the incompressibility limit for most cases, this definition is assumed to be valid for the present study. The second blowing coefficient used in this study is the power coefficient, C_π, which is defined as[21] $C_\pi = \frac{Q*P}{\frac{1}{2}*\rho_\infty*A_{ref}*U_\infty^3}$, where Q is the volumetric flow rate to the actuators and P is the static pressure inside the actuator plenum. This coefficient allows one to evaluate the efficiency of an actuation system in terms of required power. Although C_π and C_μ are proportional for most cases, C_π becomes important when the actuator geometry is modified. Therefore, we will report the C_π results only for the cases where there is a variation in the actuator internal geometry, which results in a different power requirement.

The actuator operation mode is defined as the three different blowing types obtained using the same actuators.[12,13] In the first mode, the SWJ actuators were operated in normal mode where oscillating jets are emitted at the exit. The oscillating jet swept back and forth between the exit-side walls generating highly unsteady jets. In the second operation mode, one of the feedback loops was blocked and the SWJ actuators emitted steady angled jets at the exit. This type of blowing generates streamwise vortices; therefore, is referred to as VGJs in the literature. In the third operation mode, the SWJ actuators emitted steady straight jets similar to tangential blowing. The steady straight jet was accomplished by a slight modification to the SWJ actuator geometry as described in Ref. 13. Consequently, all three active flow control methods were obtained using the same actuators, which enabled a direct comparison of three different flow control methods.

The effect of actuator placement was studied by varying the pitch angle (α), spreading angle (θ), and the streamwise location (X_{SWJ}) of the SWJ actuators. The pitch angle, which is the angle between the jet axis and the local flow in the vertical plane, was varied from 30° as the baseline to 16° and 45° using commercially available angle blocks. One surface of the angle block was attached to the actuator-top surface and the other surface was attached to the splitter plate. Since the splitter plate was parallel to the free-stream flow at Station 58, the accuracy of the pitch angle was assured using the angle blocks. Although the pitch angle could be well defined and its installation was straightforward, the spreading angle of an SWJ actuator is affected by the fluid interactions inside the actuator and therefore not easy to control. The spreading angle is analogous to the skew angle of a VGJ actuator; however, the skew angle of a VGJ actuator is usually constant but the skew angle of an SWJ actuator varies repetitively while the jet oscillates at the exit. In addition, the spreading angle of an SWJ actuator represents the time averaged skew angle at each side of the actuator centerline. The easiest way of reducing the spreading angle is to reduce the opening angle of the actuator exit so that the jet spreading is confined between the exit sidewalls. However, in our study, we noticed that when the jet exit was located at the actuator throat, the spreading angle was also limited. Usually, the throat of an actuator is desired to be closer to the local flow to eliminate any further losses. Therefore, we chose this arrangement rather than the former to show that designing the actuator exit at the actuator throat may not always be the best option for the SWJ actuators. The third parameter associated with the actuator placement is the streamwise location of the SWJ actuators, X_{SWJ}. It has been known that active flow control methods work best when they are placed close to the flow separation location. In order to study the effect of the actuator location, we compared two cases where the actuator array was installed at Station 58 and Station 62. Note that since Station 62 was on the ramp section, the pitch angle (α) was different from that of the baseline case.

The effect of actuator size on the actuator performance was investigated by varying the aspect ratio and the scale of the SWJ actuators. The aspect ratio (AR) was defined as the ratio of the width to the depth of the actuator throat and determined to be 2 for the baseline case. The AR was reduced to 1 by increasing the actuator depth to 0.25 inch and increased to 4 by reducing the actuator depth to 0.0625 inch while keeping the actuator planform geometry the same. The effect of AR was also studied previously in Ref. 13 with different actuator configuration but without considering the actuator power requirements. The actuator scaling was studied by reducing the actuator size based on its throat dimensions without changing the aspect ratio or any other parameters. The baseline actuator had 0.25 inch x 0.125 inch throat size (1X scale). This size was scaled down to 0.15 inch x 0.075 inch (0.6X scale), and 0.075 inch x 0.038 inch (0.3X scale), respectively. Reducing the actuator size required more pressure, i.e., more power, to maintain the same momentum coefficient. Therefore, the power coefficient, C_π, was also used in comparisons to incorporate the power requirement of different sized actuators. In addition, velocity profile measurements of the SWJ actuators with different sizes were obtained to show how the actuator's jet-velocity was affected by actuator size.

III. Results and Discussion

A. Separated Flow and Reference Flow Control with MVGs

All of the experiments in this study were performed at a free-stream velocity, U_∞, of 140 feet/second. This corresponded to an approximate Mach number of 0.12. The boundary-layer thickness (δ) and the momentum thickness at Station 57 were previously reported to be 0.87 inch and 0.097 inch, respectively. The Reynolds number based on the momentum thickness was 6600. Figure 3 shows a typical centerline C_p distribution of the separated flow on the APG ramp without flow control. The no flow control (NFC) case was tested several times to check data repeatability. The maximum standard deviations were observed mostly at the upstream stations near the suction peaks and measured to be less than 0.2%. The standard deviations were less than 0.06% for the downstream regions where flow separation was observed. The NFC case has a suction peak near Station 60 followed by a decrease in suction pressure due to the adverse pressure gradient. The C_p distribution indicates flow separation near Station 64 where a sudden change (plateauing) in the pressure distribution occurs. Downstream of Station 72, the centerline suction pressure continues to drop as the separated flow re-attaches to the ramp surface. The effect of MVGs on the C_p distribution is also shown in this figure. The MVG data represents a target C_p distribution to be achieved by the SWJ actuators. Strong vortices generated by MVGs reduce the influence of the sidewall vortices and allow the centerline flow to remain attached as the suction pressure gradually decreases under the influence of APG. MVGs increase the upstream suction pressure slightly and provide substantial pressure recovery by eliminating flow separation.

Figure 4 shows contours of spanwise vorticity with in-plane velocity vectors on the centerline of the ramp for the NFC case. The freestream flow is from left to right as shown by the velocity vectors and the gray area represents the APG ramp model. As indicated by the vorticity contours, the shear layer separates near Station 64 consistent with the C_p distribution. The reversed-flow line in this figure indicates flow reattachment near Station 71. A thin reversed-flow region (approximately 0.2δ maximum thickness) is expected because the Stratford ramp is designed to generate an APG that causes minimum shear stress over the pressure recovery region. The magnitude of the near-wall vorticity in the reversed-flow region is substantially less than that of the attached flow. Discrete local reversed-flow regions are observed near flow separation (Station 64) due to the thin reversed-flow region. Since the field of view was relatively large covering the entire ramp section, the camera resolution was not sufficient to capture the details of this thin region near the wall. In addition, the surface glare and the surface curvature also limited the near-wall velocity measurements. The same holds true for the discrete reversed flow regions near flow reattachment. Low-magnitude vorticity is observed near the reattachment location where the shear stress is minimal. The vorticity level gradually increases as the centerline flow fully re-attaches to the ramp surface.

Surface flow visualization of the NFC case is presented in Fig. 5. In all flow visualization figures, the flow direction is from top to bottom and the longitudinal stations are labeled on the side. This flow visualization image is very similar to Fig. 7 in Ref. 4; however, the new flow visualization technique provides more detail about the flow structures, especially in the separated flow region. In addition, this new technique required small amounts of mixture (0.35 fl. oz. to cover a 15 inches x 20 inches area); therefore, it did not lead to excessive collection of oil mixture, especially in the spiral nodes and tunnel corners. The image shows two large corner vortices on the upper portion of the ramp as indicated by two spiral nodes. Consistent with the C_p distribution and PIV measurements, the oil mixture appears to be collected near Station 64 indicating a flow separation location. In this figure, there is another oil collection site located near Station 67, where due to the ramp inclination and the reversed flow, the gravitational and shear stress forces compete with each other. Therefore, this second oil accumulation site can be interpreted as the location where gravity and the shear stress balance each other. The center of the reattachment node is located approximately at Station 71.5. Consistent with the PIV measurement, oil movement near the reattachment node is minimal due to the low shear stresses. The separated flow is highly three dimensional because of the interaction between the reversed flow, the corner vortices, and the reattachment node.

Figure 6 shows the surface flow visualization of the MVG flow control case. The red lines on top of the figure illustrate only the spanwise distribution of MVGs not the streamwise location. Strong vortices generated by MVGs eliminated flow separation and maintained attached flow in the majority of the domain. The corner vortices could be seen in the domain because the six-MVG configuration acted only on a 7.5-inch wide region at the tunnel center. However, compared to the NFC case, these corner vortices have larger footprint in the streamwise direction due to the attached flow in-between. Six-MVG configuration generated six counter rotating streamwise vortices. Usually, the counter-rotating vortices are classified based on the common flow in-between. They are referred to as "common-flow-down" when the common flow is directed toward the wall and "common-flow-up" when it is directed away from the wall. Two counter-rotating vortices generated by inverted **v**-shaped MVGs were in common-flow-down configuration that brought higher-momentum fluid from the outer boundary layer toward the

wall. On the other hand, two counter-rotating vortices generated by **v**-shaped MVGs were in a common-flow-up configuration that caused the local flow to lift off the ramp surface as indicated by the longitudinal flow detachment lines. The flow-detachment lines appear as dark lines when the circulation of the counter-rotating vortices are strong enough to lift the oil material off the surface or appear as stagnant oil lines when the counter-rotating vortices cancel each other's effect. On each side of centerline near Station 64 along the flow-detachment lines, there are two small regions of recirculating flow formed by the common-flow-up vortex pairs. Interestingly, their locations perfectly match with the flow separation location. Here, the boundary layer is thicken by the flow directed away from the wall, separates locally under the effect of APG, and generates these pockets of recirculating regions. A similar structure was also observed downstream of the common-flow-up vortex pairs with high profile VGs in experimental[5] and numerical[22] studies. The stagnant oil upstream and downstream of these pockets indicates the flow-detachment line. Spacing between two-detachment lines was 2.5 inches that was the spacing between two **v**-shaped MVGs; however, these pockets were approximately 2-inches apart due to the corner vortices. It should be noted that previously reported flow visualization results for the same ramp model in Ref. 4 showed attached flow without any recirculating regions. This is because the orientation of the MVGs in that study generated co-rotating vortices, which would not generate these recirculating regions. In addition, the number of MVGs was greater and the spacing was smaller (14 MVGs with 0.5-inch spacing), which influenced both the corner vortices and the flow in-between. Although MVGs are preferably located near suction peaks to generate stronger vortices, the MVGs in this study were located at this particular location to make an unbiased comparison with other cases.

B. The Effect of C_μ and the Baseline Case

The effect of the momentum coefficient (C_μ) was studied first to find a baseline value for C_μ to be used with other parameters. Beginning from a low flow rate (C_μ = 0.1%), C_μ was gradually increased to achieve the target C_p distribution of the MVG control. Figure 7 shows that C_μ has a significant impact on the C_p distribution. Higher C_μ values resulted in a higher upstream-suction peak and more downstream-pressure recovery. A C_p distribution comparable to that of the MVG flow control case was produced for C_μ = 0.4%. Therefore, C_μ = 0.4% was inferred to be the minimum needed to recover the pressure losses due to flow separation on the APG ramp and was used as the baseline C_μ value in this study. Excessive blowing resulted in additional pressure recovery; however, the efficiency of the actuator system was greatly reduced.

Figure 8 shows time-averaged contours of spanwise vorticity with in-plane velocity vectors obtained on the centerline for the baseline case. The baseline case maintained attached flow over the APG ramp using the following parameters: C_μ = 0.4%, α = 30°, θ= 120°, X_{SWJ} = Station 58 and AR = 2. We observed negative near-wall vorticity for the entire region, which is typical of attached flow. Figure 9 shows the surface flow visualization for the baseline case. Compared to the other flow visualization results, the flow pattern was visualized about 0.5-inch downstream of the SWJ-actuator exits to observe how the generated vortices travel downstream before reaching the APG region. The vortices generated at the actuator exit traveled downstream and maintained attached flow in the entire region. The two large corner vortices appear on the upper portion of the ramp. Their sizes were similar to that of the MVG case since no attempt was made to control them. In addition, since each SWJ actuator generates one counter-rotating vortex pair,[13] the generated vortex configuration is similar to the MVG case. In other words, the same number of vortices with the same rotation was generated at the same locations. Although the generated vortices were very similar to that of MVGs, we did not observe any small pockets of recirculating flow. The clear detachment lines in this figure indicate that the vortices generated by the SWJ actuators may be stronger than the MVGs. Furthermore, the common-flow-up vortices generated by the SWJ actuators are out of phase so they do not cancel each other's effect.[13] Note that the clear flow detachment lines between two SWJ actuators denote only the time-averaged vortices generated by the SWJ actuators. Instantaneously, the SWJ actuators generate vortices in the entire region between the actuator-exit sidewalls due to the constant jet oscillation. In contrast to the MVG control case where steady streamwise vortices were generated, the spanwise-varying vortices generated by the SWJ actuators reduce any local boundary layer growth thereby eliminating any stagnant oil flow region.

C. The Effect of Actuator Operation Modes

The actuator operation mode refers to operating the same actuator in a different way to obtain three well-known active flow control methods. These three active flow control methods are steady-straight jet (STJ), steady-angled jet (VGJ) and unsteady-oscillatory jet (SWJ). The SWJ actuators with AR=2 were used to produce the three types of jets and all other parameters were set to their baseline values. Using the same actuator for both steady and unsteady jets enables a more direct comparison since it eliminates possible variations in actuator parameters such as location, orientation, orifice spacing, A_{jet}, and others, which may lead to biased conclusions. The three operation modes only

required a slight modification in the internal actuator geometry (such as blocking the feedback loops); therefore, the exit jet velocities were the same but there were some variation in the plenum pressures. The plenum pressures for the same momentum coefficient (C_μ = 0.4%) were 1 psid, 0.85 psid, and 0.69 psid for the SWJ, VGJ, and STJ modes, respectively. As expected, blocking the feedback loops reduces the pressure losses inside the actuator. The C_p distribution in Fig. 10 shows the comparison of these three flow control methods for C_μ = 0.4%. This figure and the remaining C_p distribution figures will focus on the separated flow region between Stations 64 and 75. The C_p distribution indicates an offset between the VGJ and SWJ actuators in the entire separated flow region. The superiority of the SWJ actuators over the VGJ actuators was attributed to the unsteady streamwise vortices generated by the SWJ actuators on both sides of the actuators, whereas the VGJ actuators generated steady vortices only on one side. These unsteady and additional vortices resulted in increased coverage, more pressure recovery, and reduced flow separation.[13] Consistent with data reported previously, the STJ actuators are the least effective method because they energize the boundary layer only by momentum addition. On the other hand, the VGJ and SWJ actuators generate streamwise vortices that provide more pressure recovery by distributing the high-momentum fluid in the boundary layer through mixing.

Different operation modes required different plenum pressures to keep the momentum coefficient the same, therefore the effect of the operation mode was also evaluated at a fixed power coefficient, C_π. The tunnel parameters were constant for all cases; therefore, C_π was kept constant by fixing the product of the plenum pressure and the actuator volume flow rate (i.e., Q*P). This product indicates the power consumption of the actuators. With C_π fixed at 0.8%, C_μ for the VGJ and STJ actuators increased to 0.45%, and 0.50%, respectively. Correspondingly, the higher C_μ values resulted in higher jet exit velocities (Table 1). Since C_μ of the SWJ actuators was the same as the baseline case, the C_p distribution for the SWJ actuator again matches very well with the MVG control case (Fig. 11). The C_p distribution for the STJ actuators appears similar to that shown in Fig. 10 but with a slightly better pressure recovery due to the increased C_μ. The VGJ actuators have a mixed impact on the C_p distribution. Although the increase in C_μ was small (10% increase), we observed better pressure recovery especially in the second half of the separated flow region. As compared to the Fig. 10 (at fixed C_μ = 0.4%), where the C_p distributions differed from the MVG (or baseline) case for the entire region, the C_p distributions with C_π fixed differed until Station 69 then both C_p distributions matched after the flow was attached. This is interesting because increasing C_μ for the VGJ actuators only affects the second half region but not the first half. As shown in the STJ case and also in the C_μ-C_p study (Fig. 7), increasing C_μ always results in a gradual increase in the pressure recovery for the entire separated flow region. To investigate this phenomenon, another study of high momentum blowing was performed. C_μ was increased to 1% for all operation modes and the results were compared to the C_μ = 0.4% case. As shown in Fig. 12, the SWJ and STJ actuators have similar trends, i.e., increasing C_μ gradually increases the pressure recovery for the entire region. Since the SWJ actuators are more effective than the STJ actuators, they provide more pressure recovery. Consistent with the previous figure (Fig. 11), increasing C_μ (2.5 times) of the VGJ actuators did not show significant promise in the first half region. The C_p distributions of C_μ = 1% and C_μ = 0.4% are very similar until Station 67 indicating that increasing C_μ does not have any effect until this station. After Station 67, the pressure recovery gradually increases as we go downstream and is comparable to that of the SWJ actuators near reattachment node.

Table 1. Actuator parameters for different operation modes.

C_π = 0.8%	*Q(cfm)*	*VR*	*P(psid)*	C_μ *(%)*
SWJ	8.8	1.6	1.01	0.40%
VGJ	9.3	1.7	0.96	0.45%
STJ	9.9	1.8	0.9	0.50%

The reason for the reduced performance of the VGJ modes can be explained by examining the flow visualization image. Figure 13 shows the surface flow visualization for the VGJ mode with all parameters set to their baseline values. Red arrows in this figure represent the location of the actuator exits as well as the blowing direction. The VGJ actuators blew steady jets toward the left-hand side creating clockwise-rotating vortices (looking upstream). Since all three actuators blew in the same direction, the vortices were co-rotating as depicted by the red curved arrows in the figure. Due to the left-hand-side blowing, we observe a bias toward that side and accompanying smaller corner vortex. As shown in this flow visualization figure, there are thicker oil flow patterns between two adjacent actuators beginning from near Station 62 and extending to Station 69. The thicker oil flow indicates low shear stress that is unable to move the oil material downstream. This region corresponds to the region where we

observed an offset between the SWJ and VGJ actuators in the C_p distribution (Fig. 11). In these regions, the VGJ actuators were unable to energize the boundary layer resulting in a thicker boundary layer (low shear stress) and causing pressure loss. Therefore, in order to recover the pressure losses between two-adjacent actuators, more actuators are required in the spanwise domain. As indicated in the C_p distribution (Fig. 12), increasing C_μ does not recover these pressure losses although it provides additional pressure recovery downstream of Station 68.

Comparison of the SWJ and VGJ actuators reveals three important findings. First of all, the VGJ actuators provide pressure recovery that is either less than or nearly equal to the SWJ actuators but not more. Second, more VGJ actuators are needed to achieve similar performance to the SWJ actuators. Third, while increasing C_μ gradually increases the pressure recovery for the SWJ actuators, increasing C_μ does not recover some of the pressure losses for the VGJ actuators. This finding may be important because it indicates that the SWJ actuators are more adaptive to the changing flow conditions than the VGJ actuators. When the flow conditions change, such as a steeper pressure gradient, the SWJ actuators can provide pressure recovery by simply increasing C_μ. However, the VGJ actuators cannot provide similar pressure recovery by simply increasing C_μ in the presence of a steeper pressure gradient but require additional actuators.

Figure 14 shows surface flow visualization results for the STJ actuators. Red arrows represent the actuator locations that blow jets parallel to the free-stream flow in the horizontal plane. Note that the jet axis had a 30° angle (pitch angle) in the vertical plane. Movement of the oil mixture due to the blown jet is indicated as darker regions near the actuator exits. A stagnant oil flow region is observed between Stations 67 and 72 indicating flow separation. We could not observe a stagnant oil flow near Station 64 possibly because the flow-driven oil "cleared out" the stagnant oil, i.e., separated flow region, although the local flow is separated. Similar oil collection was also observed in the NFC case (Fig. 5) but the oil mixture did not move further downstream due to the balance between the gravity and the local shear stress. Beginning from Station 62, we observed thicker oil flow patterns (low shear stress) due to the thicker boundary layer. Similar thick-oil flow patterns were also observed in the flow visualization of the VGJ actuators (Fig. 13). While the low-shear regions were between two adjacent actuators for the VGJ actuators, this region extends to the entire tunnel width for the STJ actuators.

D. The Effect of Actuator Placement

Actuator placement consists of the pitch angle, spreading angles and the streamwise location of the SWJ actuators. The pitch angle, α, is defined as the angle between the jet axis and the surface tangent. Since the SWJ actuators were installed upstream of the ramp where the freestream flow was parallel to the surface, the pitch angle is also defined as the angle between the jet axis and the freestream flow. Three different pitch angles, namely 16°, 30°, and 45° were evaluated using commercially available angle blocks. Figure 15 shows the effect of the pitch angle on the C_p distribution. All of the parameters except the pitch angle were set to their baseline values. The C_p distributions for $\alpha = 45°$ and $\alpha = 30°$ are very close to the MVG flow control case. We observed a slightly better pressure recovery for $\alpha = 16°$. This may be because the smaller pitch angle results in a more-tangential component of the jet blowing. This is also consistent with the previously reported data, where maximum pressure recovery on a backward-facing ramp was obtained using an array of VGJ actuators with $15° < \alpha < 25°$.[8] Very small (tangential) and large pitch angles were not evaluated in this study. For the cases tested, the C_p distribution suggests that small pitch angles are beneficial although the effect is not significant.

The second parameter of the actuator placement is the spreading angle of the SWJ-actuator jet. The spreading angle, θ, is analogous to the skew angle of a VGJ actuator, which is found to be an important parameter in the literature. As reported previously, the SWJ actuator jet oscillates between two actuator exit sidewalls and these periodic oscillations are not sinusoidal.[10, 12] In fact, the jet spends most time on the actuator sidewalls during the oscillation, which results in double peaks in the mean velocity profiles. As a result, two vortices were observed on each side of a SWJ actuator as indicated by clear flow-detachment lines in the flow visualization (Fig. 9). Although the skew angle of the SWJ actuators changes constantly, the spreading angle is defined based on the mean velocity profile. To assess the effect of the spreading or skew angle, two actuators with different spreading angles were fabricated. The velocity profile for each actuator was measured at different downstream locations using a hot-wire anemometer on a benchtop test, and then the jet-half width was used to determine the spreading angle. The spreading angles were found to be approximately 80° and 120°. Figure 16 shows the effect of the spreading angle on the C_p distribution. While the baseline case with $\theta = 120°$ matches very well with the MVG control case, note how reducing the spreading angle greatly reduces the pressure recovery in the separated flow region. The pressure recovery for both spreading angles appears to be similar downstream of Station 73 where the flow is fully attached. Since the same actuators with the same input mass flow rate were used, the reduced pressure recovery implies reduced actuator efficiency. Reduced efficiency of the SWJ actuators with smaller spreading angle is also consistent

with the results about the skew angle of VGJ actuators in the literature. Although there are mixed results about the optimum skew angle of VGJ actuators, an angle between 60° and 90° is well-suited for separation control studies on an APG ramp.[23] In another experiment, substantial pressure recovery was also achieved on a ramp using the VGJ actuators with a skew angle of 60°.[8] In addition, a variation from 60° to 90° in the skew angle did not cause significant changes in the overall flow features.[24] Although we could not test the SWJ actuators with 180° spreading angle, for the cases tested and considering the results provided in the literature about the VGJ-skew angle, we conclude that a spreading angle between 120° and 180° provides better pressure recovery and thereby better actuator efficiency.

It has been known that flow control methods that use blowing are more efficient when they are installed near the separation location.[8] To investigate the effect of the actuator streamwise location, the actuator array was evaluated at two streamwise locations, namely, X_{SWJ} = 58 (baseline case) and X_{SWJ} = 62. Usually, the actuator location is defined based on the distance between the actuator and flow separation. In terms of the boundary-layer thickness, the actuator-streamwise locations (X_{SWJ} = 58 and X_{SWJ} = 62) are 6.9δ and 2.3δ, respectively. Figure 17 shows the effect of actuator streamwise location on the C_p distribution. As shown in this figure, more pressure recovery was obtained when the actuators were installed near flow separation. Because C_μ is held constant, more pressure recovery implies the downstream actuator is more efficient. After Station 71, the C_p distributions become similar due to the attached flow. The effect is more pronounced near Station 66 due to the steeper APG. Note that the pitch angle of the downstream actuator (α = 42°) was larger than the baseline actuator (α = 30°) due to the ramp surface. However, as discussed in the previous section, the effect of the pitch angle was negligible, especially for α = 30° and α = 45°. The reason for this increased performance may be that the vortices generated by the downstream SWJ actuators still have higher circulation by the time they reach the separated flow region due to their proximity. On the other hand, the vortices generated by the upstream actuators decay as they travel downstream and by the time they reach the APG region, they do not have enough circulation to energize the boundary layer. In addition, the upstream actuators energize the boundary layer before it is subjected to APG, whereas, the downstream actuators directly energize the boundary layer that is decelerated by APG.

Although the C_p distributions clearly showed the effect of the actuator placement, the flow visualization helps to better understand why the smaller spreading angle provides inferior actuator efficiency. As shown in this flow visualization figure (Fig. 18), the ramp flow seems to be attached in the majority of the domain. When compared to the baseline case (Fig. 9), the flow-detachment lines are not as clear. This suggests that the generated vortices are not as strong as the baseline case due to the reduced skew or spreading angle. In addition, the actuators are effective on relatively limited area (about 1-inch wide area for each actuator). This is expected because the spreading angle directly related to the actuator's coverage area. Although the boundary layer is energized and the flow appears to be attached, we observe thicker oil flow patterns beginning from Station 62 between two adjacent actuators. The thicker oil patterns indicate a low shear stress region. These low shear stress regions and the regions that were influenced by the actuators) are distinctly seen side by side downstream of the actuators. The low shear stress regions seem to be about 1.2 inches wider. This low shear stress region may be the reason for the reduced pressure recovery for the SWJ actuators with smaller spreading angles.

Figure 19 shows the flow visualization for the downstream actuators (X_{SWJ} = 62). Comparing this figure with the baseline case (Fig. 9, X_{SWJ} = 58) reveals the effect of the actuator location. Since more pressure recovery was achieved with C_μ = 0.4% than the baseline case in Fig. 17, the momentum coefficient was reduced 50% (C_μ = 0.2%) for this particular case. The flow visualization begins from Station 63 immediately downstream of the actuator exits. The counter-rotating vortex pairs appear to merge near Station 64.5 and maintain attached flow even with half C_μ. Another noticeable difference is the clear flow detachment lines in the APG region for downstream actuator that were not observed in the APG region for the baseline (upstream actuator) case. This also indicates the reduced strength of the vortices generated by the upstream actuator by the time they reach the APG region.

E. The Effect of Actuator Size

The effect of the actuator size on the actuator performance was studied by varying the aspect ratio and scaling of the SWJ actuators. As mention previously, the aspect ratio (AR) is defined as the ratio of the actuator throat width to actuator throat depth. The aspect ratio for the baseline configuration was 2 with a 0.25-inch wide by 0.125-inch deep throat. The aspect ratio was reduced to 1 (AR1) by increasing the depth to 0.25 inch and then increased to 4 (AR4) by reducing the depth to 0.0625 inch while keeping the actuator planform geometry the same. AR is important because it is directly related to the power/mass consumption of the actuators. In addition, the actuator velocity profiles and the generated vortices may have different structures. The relevant actuator parameters for different aspect ratios are given Table 2. The effect of AR on the actuator performance was previously studied on a

similar ramp model with a different actuator location and the AR4 actuators were reported to produce less pressure recovery.[13] Without knowing the actual reason for the reduced performance, it was speculated that a smaller-orifice jet requires a relatively longer distance to penetrate through the boundary layer, although it generates a stronger vortex.[25] To test this hypothesis, the SWJ array was installed at Station 58 in this study to provide more distance compared to the previous study. Figure 20 shows the effect of AR on the C_p distribution for fixed C_μ = 0.4%. All other parameters were set to their baseline values. As depicted in this figure, all of the AR cases resulted in substantial pressure recovery compared to the NFC case. The AR2 and AR4 actuators produced almost identical C_p distributions. This finding is very important because the AR4 actuators require almost 30% less flow rate (Table 2); however, the required pressure to achieve the same C_μ doubled, resulting in almost a 50% increase in C_π. On the other hand, the AR1 actuators provided less pressure recovery for the entire region despite the fact that the flow rate increased more than 40%. Note how the C_p distribution of the AR1 actuators gradually deviates from the baseline case downstream. A similar trend was also obtained in Ref. 13 for the AR1 actuators. The reason for the reduced pressure recovery and the gradual deviation from the baseline case was attributed to the vorticity produced by the AR1 actuators being weak due to its smaller velocity ratio. This weak vortex decayed earlier and reduced its effectiveness in the downstream region. Since the SWJ actuators were installed at Station 62 in the previous study, the deviations were steeper. However, in the current study, the actuators were installed at Station 58, thus the vorticity level has diminished by the time the vortices reach the APG region. Therefore, we see a gradual deviation from the baseline case compared to that of Ref. 13.

Table 2. Variation of actuator parameters with AR for a fixed C_μ.

C_μ = 0.4%	Q(cfm)	VR	P(psid)	C_π (%)	f(Hz)
AR4	6.21	2.26	2.07	1.15	238
AR2	8.78	1.59	1.00	0.78	178
AR1	12.39	1.13	0.43	0.48	110

Changing the actuator geometry while keeping C_μ the same changes the required pressure and the flow rate for the SWJ actuators (Table 2). Although C_μ is a well-known parameter to characterize the effect of different actuator configurations, another approach is to check the actuator power consumption, which may be an important parameter when deploying these actuators on aircraft components. Therefore, another study was performed using the same actuators but fixing the power coefficient to assess the effect of AR at a fixed power consumption level. Figure 21 shows the C_p distributions for the SWJ actuators with different aspect ratio at C_π = 0.8%. The relevant actuator parameters are given in Table 3. Similar trends are seen with respect to the effect of AR on the actuator performance. The AR1 actuators are the least effective and their effectiveness deviates from the other two actuators between Station 69 and Station 74. Consistent with the results of the C_μ-C_p study shown in Fig. 7, the pressure recovery for the AR1 actuator is increased compared to the fixed-C_μ study due to the increase in C_μ (0.56%). On the other hand, the pressure recovery for the AR4 actuators is reduced due to the reduction in C_μ (0.32%).

Table 3. Variation of actuator parameters with AR for a fixed C_π.

C_π = 0.8%	Q(cfm)	VR	P(psid)	C_μ (%)	f(Hz)
AR4	5.59	2.04	1.60	0.32	215
AR2	8.83	1.61	1.01	0.40	178
AR1	14.68	1.33	0.61	0.56	264

Another parameter related to the actuator size is the actuator scale. In the AR study, we kept the actuator planform geometry the same and varied the actuator depth. In this study, three different sizes of actuators were fabricated by scaling down the baseline actuators by 60% (0.6X) and 30% (0.3X), respectively, without changing the actuator spacing and streamwise location. All other parameters were set to their baseline values. Comparison of the C_p distributions for the actuators with different scales indicates substantial pressure recovery (Fig. 22) for all cases. The baseline configuration provided slightly better pressure recovery and both of the scaled-down actuators resulted in identical pressure distribution. Although the required flow rate reduces linearly with the actuator scale, the required pressure to supply the same C_μ increases greatly for small-scale actuators (Table 4). Similar to the AR study, we also evaluated the actuator performance for fixed C_π=0.8% because the actuator modification requires different power/mass to operate them. As shown in Fig. 23, the baseline actuator provided the most pressure

recovery and the smallest sized actuator provided the least. This is because C_μ gradually reduces (Table 5) as the actuator size is reduced thereby providing less pressure recovery compared to the fixed-C_μ data in Fig. 22.

Table 4. Variation of actuator parameters with scale for a fixed C_μ.

C_μ = 0.4%	Q(cfm)	VR	P(psid)	C_π (%)	f(Hz)
0.3X	2.64	5.32	5.63	1.33	1537
0.6X	5.25	2.65	2.31	1.09	406
1.0X	8.78	1.59	1.00	0.78	178

Table 5. Variation of actuator parameters with scale for a fixed C_π.

C_π = 0.8%	Q(cfm)	VR	P(psid)	C_μ (%)	f(Hz)
0.3X	2.18	4.41	4.09	0.27	1325
0.6X	4.80	2.42	1.85	0.33	375
1.0X	8.83	1.61	1.01	0.40	178

In order to see the global effect of the actuator size on the flow field, we performed surface flow visualization. Figure 24 shows the flow visualization results obtained using the 0.6X-SWJ actuators with C_μ set to 0.4%. Consistent with the C_p distribution, we obtain very similar flow patterns to the baseline case (Fig. 9). The vortices produced by the SWJ actuators traveled downstream and generated clear flow-detachment lines. These flow-detachment lines appear to merge at Station 61.5 similar to the baseline case. The generated vortices energized the boundary layer and hence maintained attached flow over the entire ramp. The lateral extent of the actuator, i.e., the jet spreading, seems to be similar to the baseline case (Fig. 9). Figure 25 shows the flow visualization for the smallest-sized actuators (0.3X actuators) with C_μ set to the baseline 0.4% value. Although the C_p distributions indicated similar performance to the large-scale actuators, the flow visualization figures show some differences. As shown in this figure, the oil flow patterns near the tunnel centerline show attached flow primarily due to the middle actuator, which was located at the tunnel centerline. Therefore, the C_p distribution of the smallest sized actuator was very similar to the large-scale actuators (Fig.22). Between Stations 62 and 65, the flow visualization shows low-shear regions due to the thicker boundary layer between two adjacent-actuators (about 1.25-inch wide area). Near Station 65, the counter-rotating vortices merge and hence maintain attached flow downstream. Similar low-shear regions were also observed in the flow visualization figures of the VGJ actuators (Fig. 18) and the SWJ actuators with small spreading angle (Fig. 12). These low-shear regions between two-adjacent actuators indicate areas where the actuators may not be able to energize the local boundary layer. As shown at the top of the figures, the lateral extent of the actuators, i.e., the jet spreading, is limited compared to the baseline or 0.6X actuators. The actuators act on about a 1-inch wide area downstream of each actuator; therefore, more actuators are needed between two actuators to energize the boundary layer and hence to eliminate pressure losses at these low shear regions. In addition, compared to the baseline or 0.6X actuators, the flow-detachment lines generated by the counter-rotating vortices are not very clear indicating that these vortices are somewhat weaker than those generated by the larger scale actuators.

Figures 26 and 27 show the effect of the actuator size on the mean velocity profiles for the SWJ actuators with different scales and aspect ratios, respectively. The velocity profiles were measured 0.625-inch downstream of the actuator throat on a benchtop. Since the flow direction and the hot-wire probe axis were not parallel, pitch corrections were applied to the hot-wire measurements as described in Ref. 12. The flow rate to the actuators were adjusted to produce the same momentum coefficient (C_μ = 0.4%). The velocity profiles were nondimensionalized by the local maximum of the jet velocity. Although the spanwise distribution of the velocity profiles is usually nondimensionalized by the actuator throat, we kept it dimensional to assess the lateral extent of the actuator's effect. All velocity profiles exhibit double peaks, which are typical of the SWJ actuators. As shown in Fig. 26, the velocity profiles of 1X and 0.6X actuators are identical, which is consistent with the C_p distributions as well as the flow visualization where both actuator configurations produced similar surface flow patterns. Although the C_p distribution showed similar performance for the smallest-sized actuator (Fig. 21), the surface flow pattern indicates that the 0.3X actuator is effective only in a limited spanwise region. The velocity profile of the 0.3X actuator shows that the actuator produces a relatively narrow jet.

Similar conclusions can be drawn for the effect of AR on actuator performance. Large and medium sized actuators (AR1 and AR2) produced identical velocity profiles while the smallest-sized actuator (AR4) produced a

narrow velocity profile indicating that the AR4 actuator is effective in a limited spanwise region similar to the 0.3X actuator. Although the centerline C_p distribution of the AR1 actuator showed reduced pressure recovery, this reduced performance was attributed to the weaker vortices generated by the AR1 actuator due to the reduced jet velocity. However, in terms of lateral extent, both AR1 and AR2 actuators have similar coverage. Although no flow visualization was obtained for the AR4 actuators, we expect a similar flow visualization to that of the 0.3X actuators (Fig. 26).

IV. Conclusion

An experimental study was performed to investigate the effect of different actuator parameters on the effectiveness of sweeping jet (SWJ) actuators to control flow separation on an adverse pressure gradient ramp model. The parameters investigated were the actuator operation mode, actuator placement and actuator size. Surface pressure measurements and surface oil flow visualization were used to determine the effects of each parameter on actuator performance. For select cases, 2D PIV measurements of the ramp flow and hot-wire measurements of the actuator's jet flow were also obtained. An array of MVGs was used on the ramp as a passive flow control device and the resultant C_p distribution was used as a target C_p distribution to be achieved by the SWJ actuators. The effect of actuator momentum coefficient (C_μ) was studied and revealed that C_μ has a significant impact on the actuator performance, providing more pressure recovery as C_μ is increased. For C_μ = 0.4%, the target C_p distribution was achieved and attached flow was maintained. The SWJ actuators with C_μ = 0.4% was used as a baseline and the effect of other parameters were characterized by comparing the pressure distribution and the surface flow patterns to that of the baseline case.

First, the SWJ actuators were compared to two other well-known active flow control methods, namely straight (STJ) and vortex generating jets (VGJ) with the same configurations. These three different blowing methods were obtained by operating the same actuators with different modes. The C_p measurements and the flow visualization indicated that the STJ actuators are the least effective because they energize the boundary layer only by momentum addition. On the other hand, the VGJ and SWJ actuators generate streamwise vortices that provide more pressure recovery by distributing the high-momentum fluid in the boundary layer through mixing. The superiority of the SWJ actuators over the VGJ actuators was attributed to the unsteady (spanwise-varying) streamwise vortices generated by the SWJ actuators on both sides of the actuators, whereas the VGJ actuators generated steady streamwise vortices only on one side. These unsteady and additional vortices resulted in increased coverage, more pressure recovery, and reduced flow separation. The flow visualization of the VGJ actuators exhibited local low shear regions between two adjacent VGJ actuators where the generated streamwise vortices were unable to energize the boundary layer. Therefore, in order to recover the pressure losses between two-adjacent actuators, more actuators are required in the spanwise plane. Comparison of the SWJ and VGJ actuators also revealed another important finding. While increasing C_μ gradually increases the pressure recovery for the SWJ actuators, increasing C_μ does not recover some of the pressure losses for the VGJ actuators. This finding may be important because it indicates that the SWJ actuators are more adaptive to the changing flow conditions than the VGJ actuators.

The effect of the actuator placement was studied by varying the pitch angle, spreading angle and streamwise location of the SWJ actuators. Since the placement of the actuators is not related to the actuator mass flow input, an increase in the actuator performance directly implies an increased actuator efficiency. Although the effect of the actuator pitch angle is small on the actuator performance, the spreading angle is found to be an important parameter and reducing the spreading angle greatly reduces the pressure recovery in the separated flow region thereby reducing actuator efficiency. The effect of the spreading angle is twofold. First, the spreading angle is directly related to the actuator spanwise coverage; therefore, the actuators with small spreading angles require more actuators or flow rate to achieve similar performance. Second, the spreading angle is also related to the skew angle of a jet described in the literature. As such, we would expect an actuator with a small spreading angle to generate vortices with low circulation levels and actuators with large spreading angles to generate vortices with high circulation levels. By investigating the actuator performance at two streamwise locations, we observed that the actuator performs better when placed closer to the flow separation location. This is because the generated vortices have higher circulation when they reach the separated flow region. On the other hand, the vortices generated by the upstream actuators decay as they travel and by the time they arrive at the APG region, they have less circulation to energize the boundary layer.

The effect of actuator size was studied first by varying the actuator aspect ratio (AR) while keeping the actuator width the same and then varying the actuator scale while keeping the aspect ratio the same. Since the actuators with different sizes require different pressures and flow rates to maintain the same momentum coefficient, the results were provided for a fixed momentum coefficient as well as for a fixed power coefficient. The AR1 actuators were

found to be the least effective providing substantially less pressure recovery despite having a high mass flow requirement. This was attributed to the weaker vorticity generated by the AR1 actuators for the same momentum coefficient due to the smaller jet exit velocity. The AR2 and AR4 actuators produced similar pressure recovery, but the hot-wire measurements indicated that the AR4 actuators have limited spanwise coverage which would make it difficult to energize the boundary layer between two-adjacent actuators. Similar conclusions can be drawn for the smallest-sized actuators (0.3X scaled). Although the different scaled (1X, 0.6X, and 0.3X) actuators provided similar pressure recovery, the flow visualization (as well as hot-wire measurements) indicated that the smallest-sized actuators have limited spanwise coverage and are unable to energize the boundary layer between two-adjacent actuators.

Acknowledgments

The author would like to thank the NASA Fixed Wing Project for funding this research and the following individuals for their support: Catherine McGinley, Luther Jenkins, John Lin, Latunia Melton, and Charlie Debro.

References:

[1] Bezos-O'Connor, G.M., Mangelsdorf, M.F., Maliska, H.A., "Fuel Efficiencies through Airframe Improvements," AIAA Paper 2011-3530, June 2011.

[2] Gad-el-Hak, M., and Bushnell, D.M., "Separation Control: Review," *Journal of Fluids Engineering*, Vol. 113, No. 1, 1991, pp. 5-30.

[3] Schubauer, G.B., and Spangenberg, W., "Forced Mixing in Boundary Layers," *Journal of Fluid Mechanics*, Vol. 8, No. 01, 1960, pp. 10-32.

[4] Jenkins, L., Gorton, S.A., and Anders, S., "Flow Control Device Evaluation for an Internal Flow with an Adverse Pressure Gradient," AIAA Paper 2002-0266, Jan. 2002.

[5] Lin, J., Howard, F., and Selby, G., "Small-Submerged Vortex Generators for a Turbulent Flow Separation Control," *Journal of Spacecraft and Rockets*, Vol. 27, No. 5, 1990, pp. 503-507.

[6] McCormick, D., "Shock-Boundary Layer Interaction Control with Low-Profile Vortex Generators and Passive Cavity," AIAA Paper 1992-0064, Jan. 1992.

[7] Lin, J.C., "Review of Research on Low-Profile Vortex Generators to Control Boundary-Layer Separation," *Progress in Aerospace Sciences*, Vol. 38, No. 4, 2002, pp. 389-420.

[8] Selby, G., Lin, J., and Howard, F., "Control of Low-Speed Turbulent Separated Flow Using Jet Vortex Generators," *Experiments in Fluids*, Vol. 12, No. 6, 1992, pp. 394-400.

[9] Gregory, J.W., and Tomac, M.N., "A Review of Fluidic Oscillator Development," AIAA Paper 2013-2474, June 2013.

[10] Vatsa, V., Koklu, M., Wygnanski, I., "Numerical Simulation of Fluidic Actuators for Flow Control Applications," AIAA Paper 2012-3239, June 2012.

[11] Ostermann, F., Woszidlo, R., Nayeri, C., "Experimental Comparison between the Flow Field of Two Common Fluidic Oscillator Designs," AIAA 2015-0781, Jan. 2015.

[12] Koklu, M., and Melton, L.P., "Sweeping Jet Actuator in a Quiescent Environment," AIAA Paper 2013-2477, June 2013.

[13] Koklu, M., and Owens, L.R., "Flow Separation Control Over a Ramp Using Sweeping Jet Actuators," AIAA Paper 2014-2367, June 2014.

[14] Melton, L.P., "Active Flow Separation Control on a NACA 0015 Wing using Fluidic Actuators," AIAA Paper 2014-2364, June 2014.

[15] Seele, R., Tewes, P., Woszidlo, R., "Discrete Sweeping Jets as Tools for Improving the Performance of the V-22," *Journal of Aircraft*, Vol. 46, No. 6, 2009, pp. 2098-2106.

[16] Cerretelli, C., Wuerz, W., and Gharaibah, E., "Unsteady Separation Control on Wind Turbine Blades using Fluidic Oscillators," *AIAA Journal*, Vol. 48, No. 7, 2010, pp. 1302-1311.

[17] Seifert, A., Stalnov, O., Sperber, D., "Large Trucks Drag Reduction Using Active Flow Control," AIAA Paper 2008-0743, Jan. 2008.

[18] Woszidlo, R., Stumper, T., Nayeri, C., "Experimental Study on Bluff Body Drag Reduction with Fluidic Oscillators," AIAA Paper 2014-0403, Jan. 2014.

[19] Andino, M.Y., Lin, J.C., Washburn, A.E., "Flow Separation Control on a Full-Scale Vertical Tail Model using Sweeping Jet Actuators," AIAA Paper 2015-0785, Jan. 2015.

[20] Scarano, F., and Riethmuller, M., "Advances in Iterative Multigrid PIV Image Processing," *Experiments in Fluids*, Vol. 29, No. 1, 2000, pp. S051-S060.

[21] Seele, R., Graff, E., Lin, J., "Performance Enhancement of a Vertical Tail Model with Sweeping Jet Actuators," AIAA 2013-0411, Jan. 2013.

[22] König, B., Fares, E., and Nölting, S., "Fully-Resolved Lattice-Boltzmann Simulation of Vane-Type Vortex Generators," AIAA Paper 2014-2795, June 2014.

[23.] Stillfried, F.V., Wallin, S., and Johansson, A.V., "Evaluation of a Vortex Generator Model in Adverse Pressure Gradient Boundary Layers," *AIAA Journal*, Vol. 49, No. 5, 2011, pp. 982-993.

[24.] Zhang, X., "Co-and Contrarotating Streamwise Vortices in a Turbulent Boundary Layer," *Journal of Aircraft*, Vol. 32, No. 5, 1995, pp. 1095-1101.

[25.] Rixon, G.S., and Johari, H., "Development of a Steady Vortex Generator Jet in a Turbulent Boundary Layer," *Journal of Fluids Engineering*, Vol. 125, No. 6, 2003, pp. 1006-1015.

Figures

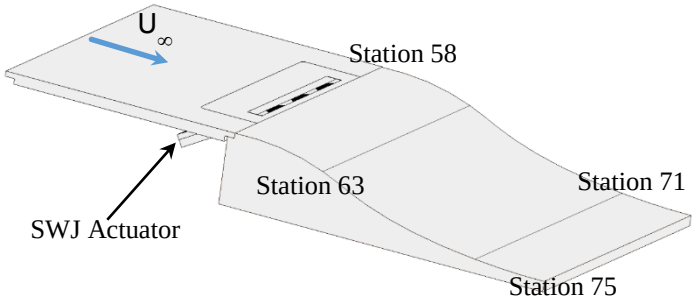

Figure 1. Schematic of the APG ramp in the tunnel.

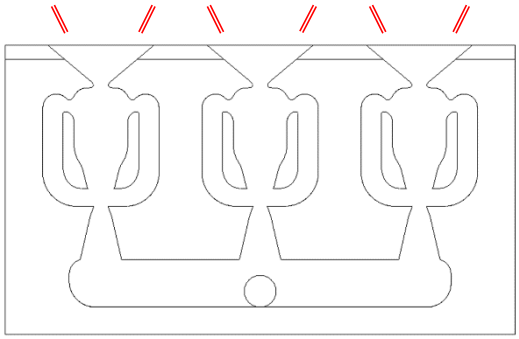

Figure 2. SWJ actuators and the spanwise distribution of MVGs relative to SWJ exits.

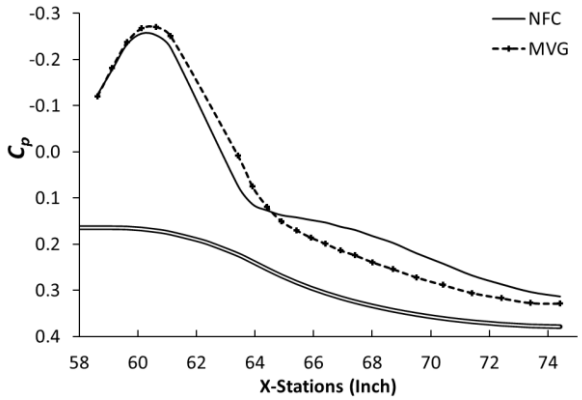

Figure 3.Centerline C_p distribution along the APG ramp for NFC and MVG cases.

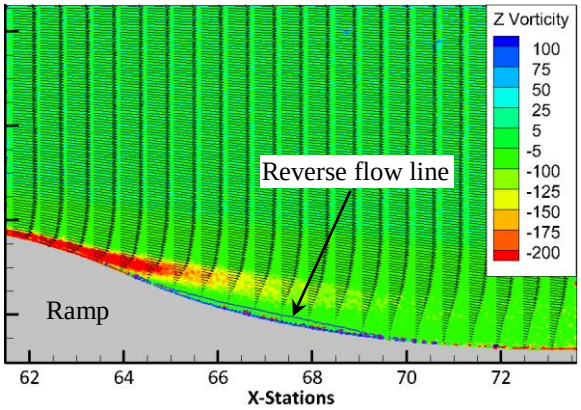

Figure 4. Contours of spanwise vorticity showing the separated flow on the APG ramp (NFC case).

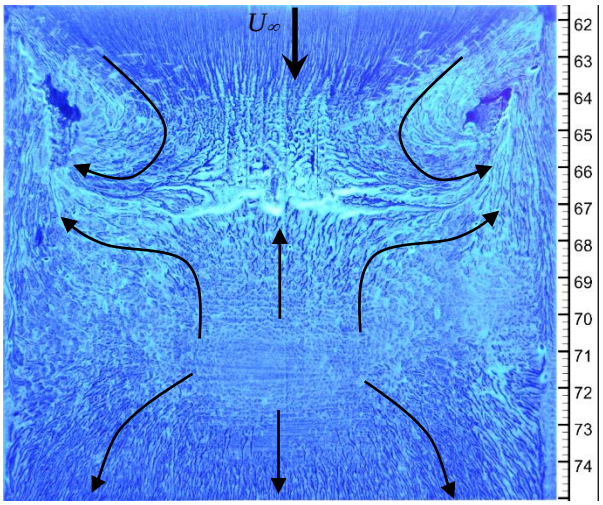

Figure 5. Surface oil flow visualization of separated flow on the APG ramp (NFC).

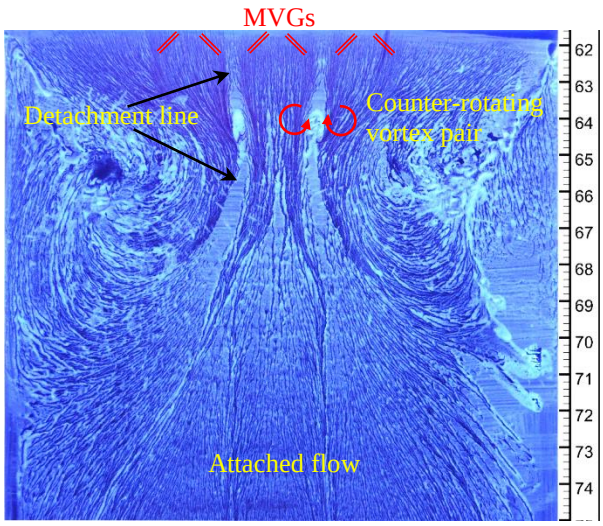

Figure 6. Surface oil flow visualization of flow control with MVGs.

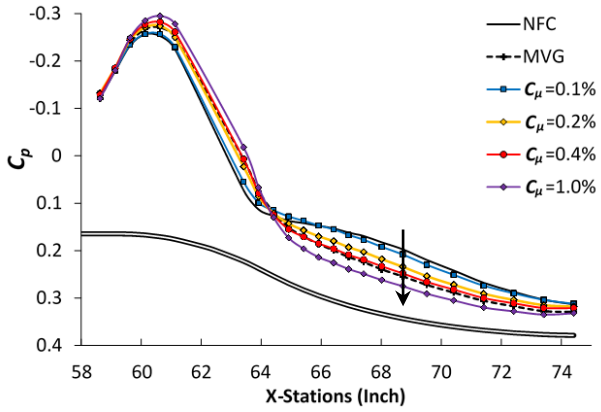

Figure 7. The effect of C_μ on the C_p distribution.

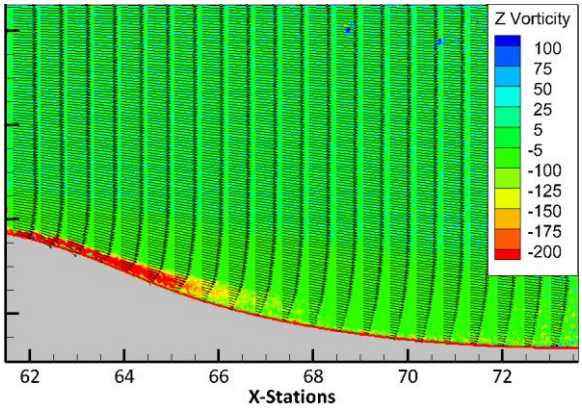

Figure 8. Contours of spanwise vorticity and in-plane velocity vectors (Baseline Case).

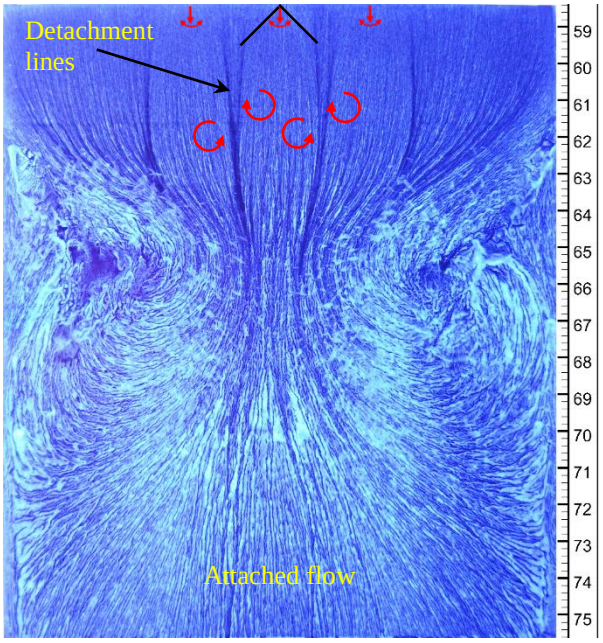

Figure 9. Oil flow visualization of the baseline case.

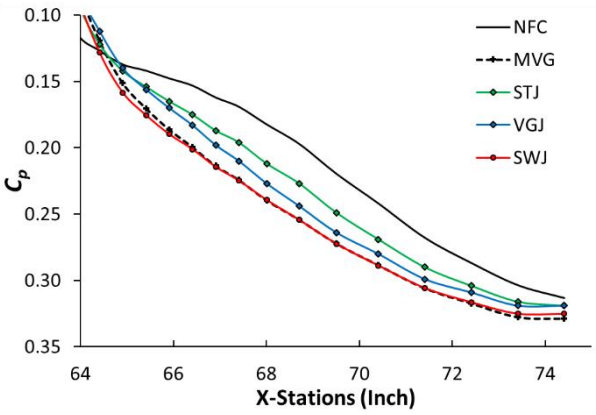

Figure 10. The effect of operation modes (C_μ=0.4%).

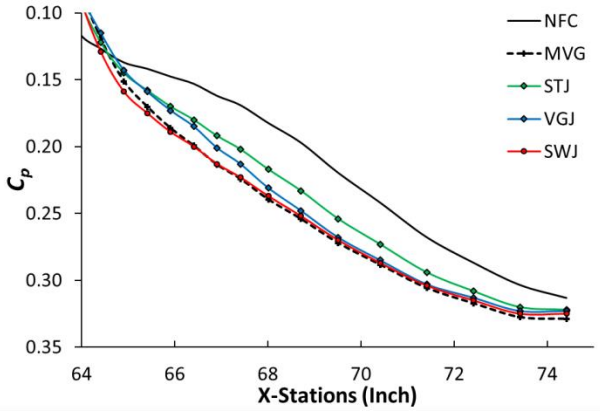

Figure 11. The effect of operation modes (C_π=0.8%).

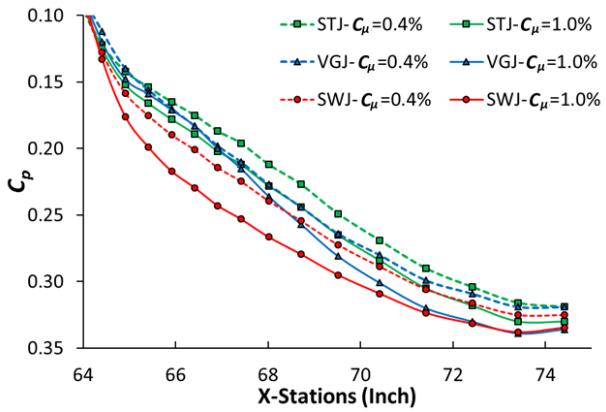

Figure 12. Operation modes at different C_μ values

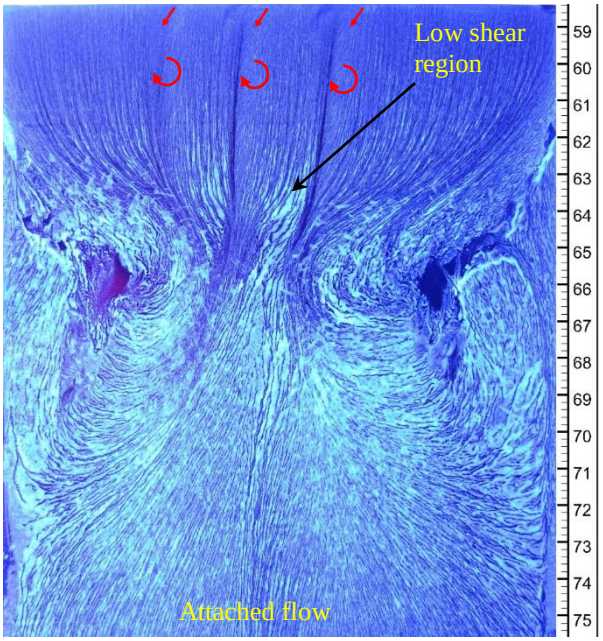

Figure 13. Oil flow visualization for VGJ mode.

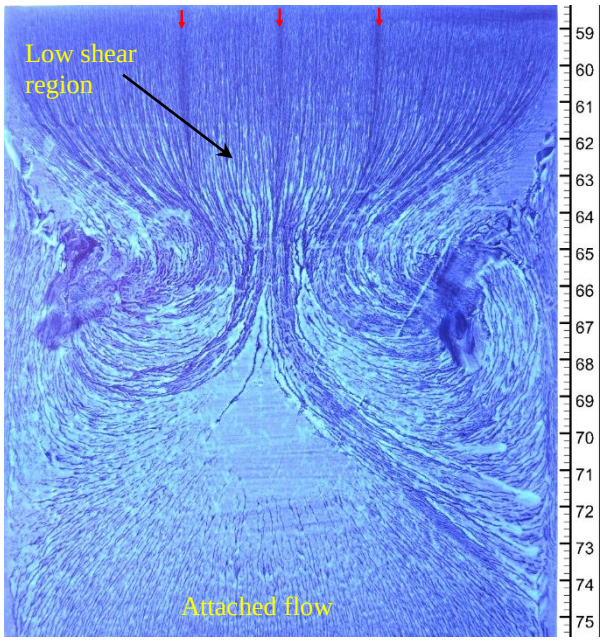

Figure 14. Oil flow visualization for STJ mode.

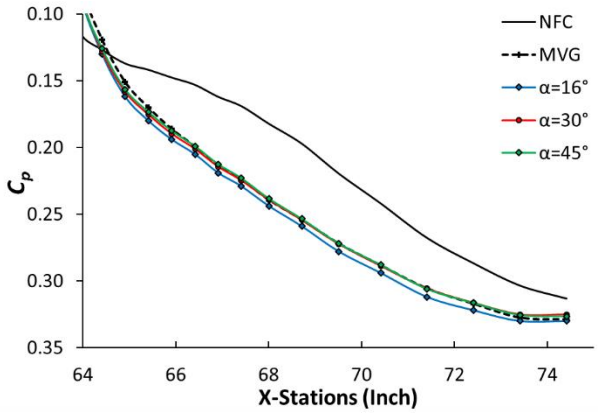

Figure 15. The effect of pitch angle (α).

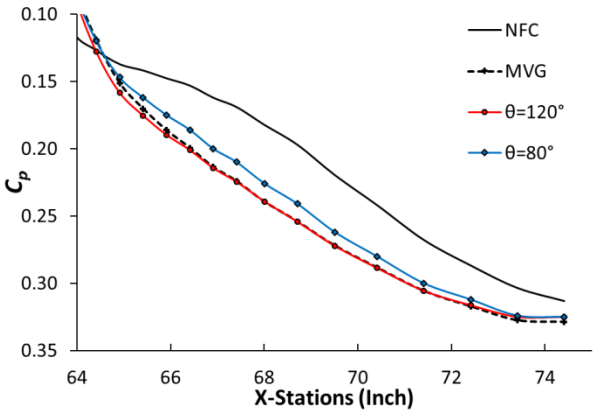

Figure 16. The effect of spreading angle (θ).

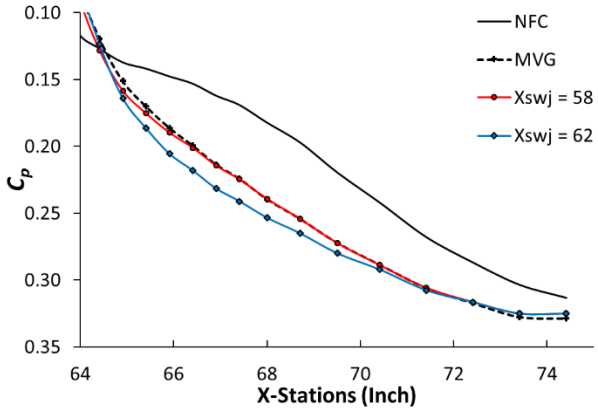

Figure 17. The effect of actuator location (X_{SWJ}).

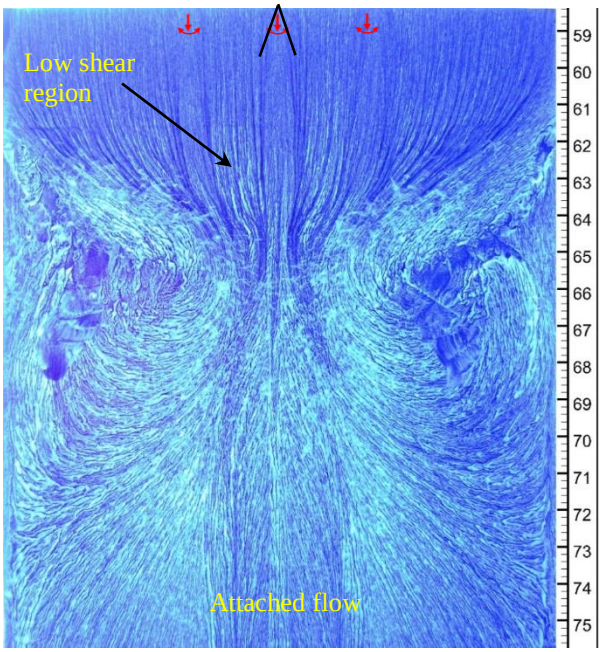

Figure 18. Oil flow visualization for θ = 80°.

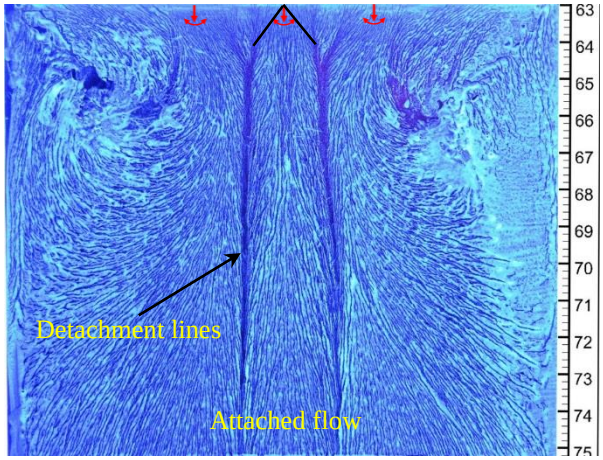

Figure 19. Oil flow visualization for X_{SWJ} = 62.

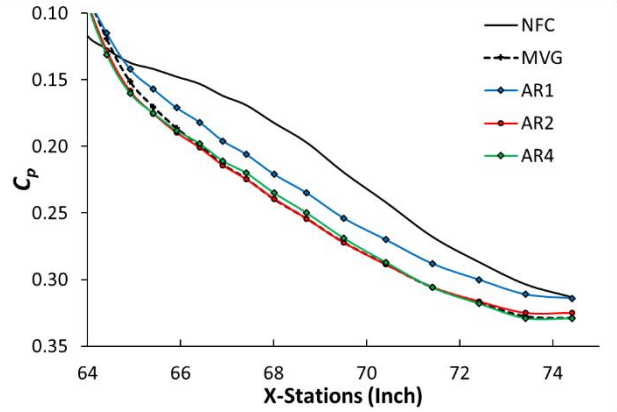

Figure 20. The effect of aspect ratio (C_μ=0.4%).

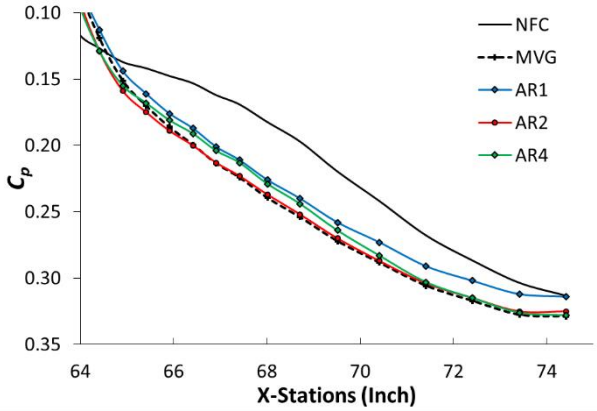

Figure 21. The effect of aspect ratio (C_π=0.8%).

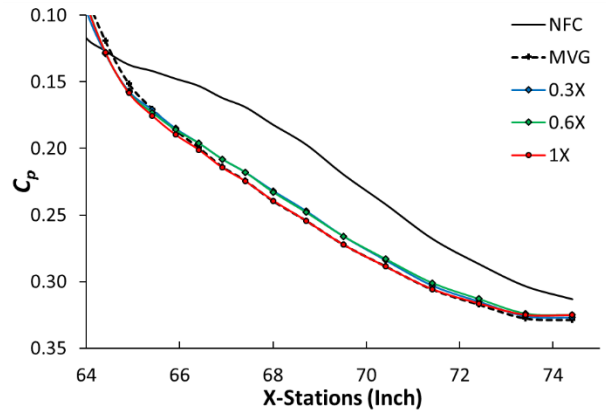

Figure 22. The effect of actuator scale (C_μ=0.4%).

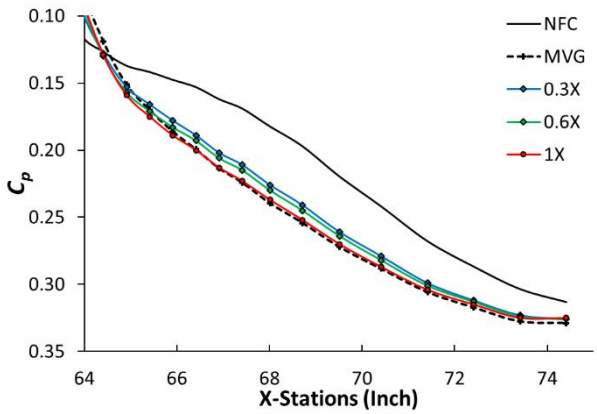

Figure 23. The effect of actuator scale (C_π=0.8%).

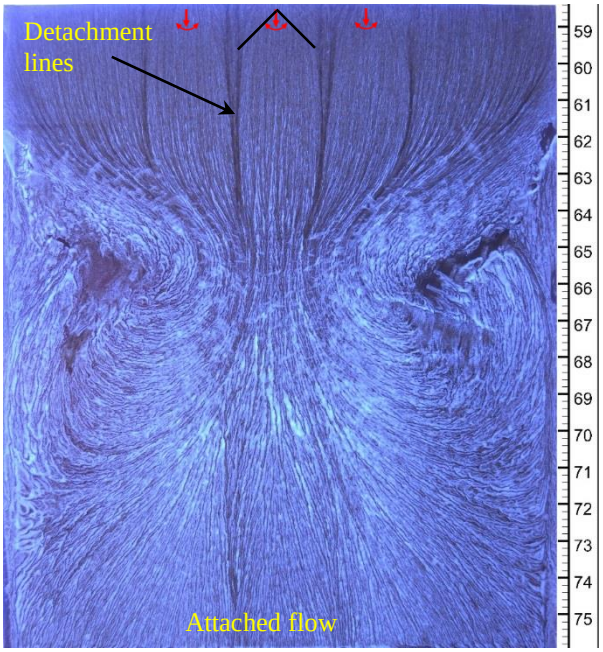

Figure 24. Oil flow visualization for 0.6X actuators.

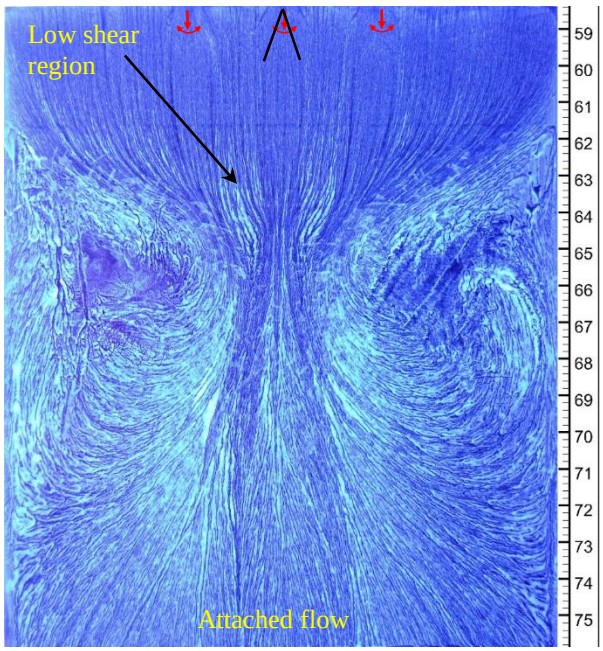

Figure 25. Oil flow visualization for 0.3X actuators.

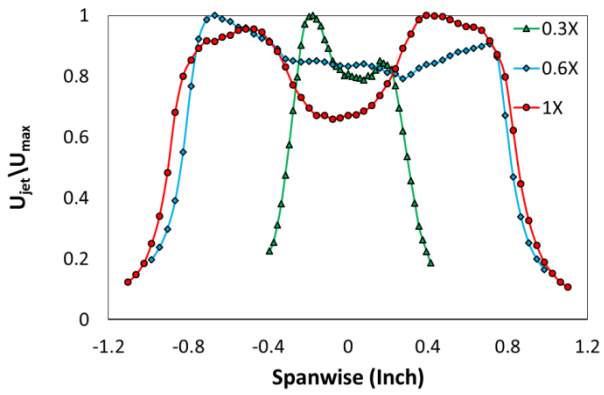

Figure 26. Actuator mean velocity profiles for different scales.

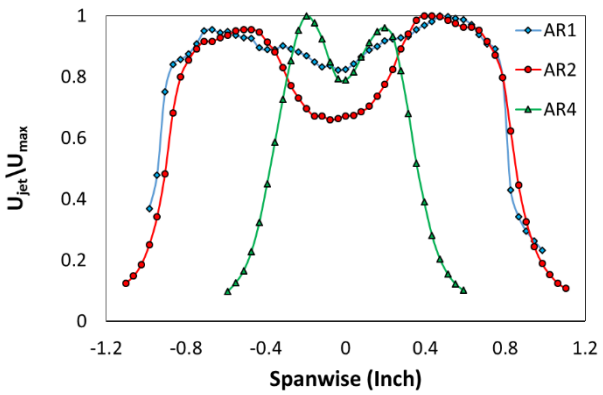

Figure 27. Actuator mean velocity profiles for different AR values.